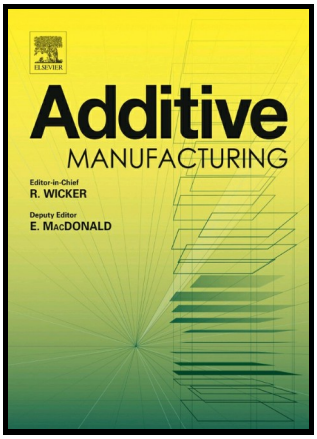

A Novel 3D Printed Hollow Microneedle Microelectromechanical System for Controlled, Personalised Transdermal Drug Delivery

Sophia N. Economidou, Md. Jasim Uddin, ManuelJ. Marques, Dennis Douroumis, Wan Ting Sow,Huaqiong Li, Andrew Reid, James F.C. Windmill, Adrian Podoleanu

PII: S2214-8604(20)31187-8

DOI: https://doi.org/10.1016/j.addma.2020.101815

Reference: ADDMA101815

To appear in: *Additive Manufacturing*

Received date:3 August 2020
Revised date:27 November 2020
Accepted date:22 December 2020

Please cite this article as: Sophia N. Economidou, Md. Jasim Uddin, Manuel J. Marques, Dennis Douroumis, Wan Ting Sow, Huaqiong Li, Andrew Reid,James F.C. Windmill and Adrian Podoleanu, A Novel 3D Printed Hollow Microneedle Microelectromechanical System for Controlled, Personalised Transdermal Drug Delivery, *Additive Manufacturing,* (2020) doi:https://doi.org/10.1016/j.addma.2020.101815

A Novel 3D Printed Hollow Microneedle Microelectromechanical System for Controlled, Personalised Transdermal Drug Delivery

Sophia N. Economidou[a*], Md. Jasim Uddin[b], Manuel J. Marques[c], Dennis Douroumis[d], Wan Ting Sow[e], Huaqiong Li[e], Andrew Reid[f], James F.C. Windmill[f] and Adrian Podoleanu[c]

[a] Medway School of Pharmacy, University of Kent, Medway Campus, Central Avenue, Chatham Maritime, Chatham, Kent ME4 4TB, United Kingdom

[b] Department of Pharmacy, BRAC University, Bangladesh. Address: 41 Pacific Tower, Mohakhali, Dhaka-1212, Bangladesh

[c] Applied Optics Group, University of Kent, Canterbury CT2 7NH, Kent, UK

[d] CIPER Centre for Innovation and Process Engineering Research, Kent, ME4 4TB, UK

[e] Wenzhou Institute, University of Chinese Academy of Sciences, Wenzhou, Zhejiang Province, 325011, P. R. China.

[f] Centre for Ultrasonic Engineering, Department of Electronic and Electrical Engineering, University of Strathclyde, 204 George St, Glasgow, G1 1XW, Scotland, United Kingdom

KEYWORDS: Microelectromechanical Systems, 3D printing; microneedles; Optical Coherence Tomography; *in vivo*

ABSTRACT

The advancement of drug delivery devices is critical for the individualization of patient treatment and the improvement of healthcare. Here, we introduce the 3DMNMEMS, a novel device that combines 3D printing, microneedles (MNs) and Microelectromechanical Systems (MEMS), allowing versatile and controllable by the user transdermal drug delivery. Hollow MNs were designed and 3D printed using Stereolithography, followed by integrating into a MEMS. By employing advanced imaging techniques, we monitored the distribution of liquid delivered by the device within skin tissue in real-time. *In vivo* testing revealed that the delivery of insulin using the 3DMNMEMS achieved improved glycemic control to diabetic animals compared to subcutaneous injections. These results demonstrated the potential of the 3DMNMEMS as a universal transdermal drug delivery system for personalized care.

1. INTRODUCTION

Personalization of clinical care is nowadays in the spotlight of research on drug delivery. Finding new pathways that allow the individualization of treatments will improve efficiency, patient compliance and limitation of adverse effects. 'Personalized medicine' is attracting worldwide interest, with sophisticated drug delivery systems being a key element [1]. Additive Manufacturing (or 3D printing) offers the unique ability of direct and fast customisation based on the application, paving the way for the development of personalized tablets, drug delivery devices, implants and advanced tissue engineering [2–7].

3D printing is an umbrella term for a group of manufacturing techniques that use virtual Computer Aided Design (CAD) models to create physical objects through a layer-by-layer fabrication process. Hence, 3D printing allows the fabrication of structures previously unattainable with conventional techniques, in a fast and user-friendly manner, while the nature of the technology simplifies and accelerates the prototyping stage. In the field of drug delivery, 3D printing is viewed as a 'new chapter' [8], having already gained visibility and recognition by the respective regulatory bodies (e.g. FDA) [9].

Transdermal drug delivery systems are attractive alternatives to oral and injection-based administration strategies since the transdermal route results in higher bioavailability, while offering the added benefit of causing minimal or no pain, thus being highly patient-compliant [10,11]. The broader use of such systems was enabled by the introduction of microneedles (MNs), which are miniature puncturing devices that surpass the outer layers of the skin tissue, achieving the delivery of a variety of molecules, proteins, DNA etc. in a minimally invasive and pain free manner [12,13]. Hollow microneedles have emerged as an alternative to typical injections, tackling issues such as pain, needle phobia and the requirement for a trained professional to perform the drug administration [14], with limited applications due to mechanical strength issues [15]. MNs are manufactured through several techniques, mainly micromoulding and micromachining which can often be multistep, time-consuming, challenging to scale-up and difficult to readapt according to individual application requirements. 3D printing is by definition a promising alternative to the traditional MN manufacturing techniques. However, there is limited progress on the applicability of 3D printing for transdermal systems recorded in the past few years [16] because its adoption in fabricating MNs has faced challenges.

The printing resolution has been a major restrictive factor. Although a high degree of fidelity between virtual and physical model is an advantage of 3D printing, high accuracy in detail formation in the microscale often exceeds the capabilities of the printer. As a consequence, issues of reliability arise, especially regarding the MN tip sharpness, which is critical for the successful insertion into the skin. Another challenge stems from the limited material palette that is readily processable with the various 3D printing technologies and is further narrowed down by the requirement of biocompatibility. Indeed, there is only a small number of biocompatible, printable materials across the whole family of printing technologies.

A small number of studies have reported the successful implementation of 3D printing as a manufacturing technique for hollow MNs, intended for transdermal purposes. Two photon polymerization (2PP), a specialised photopolymerization printing technique, has been used for the development of MN masters for micromoulding [17] as well as for the direct fabrication of patches. Ovsianikov et al. employed 2PP to fabricate hollow MNs, reporting that the manufacturing process had no adverse effects on cell viability and growth [18]. The same technology was also employed to develop a combined hollow MN and reservoir patch that can be potentially incorporated in transdermal and implantable systems [19]. The aforementioned technology favours MN fabrication due to its exceptional resolution, thereby enabling the formation of sharp MNs. However high costs, longer printing times and small printing volumes [20], hamper the production in larger numbers, raising questions regarding the technology's potential for broad clinical applications.

To overcome these challenges, exploring the applicability of more accessible printing technologies, is imperative. Recently, our group demonstrated that commercial laser Stereolithography (SLA) can be a valuable tool for fast, cost-effective and readily customizable manufacturing of biocompatible solid coated MNs with tailored drug loadings. The MNs were tested for their ability to deliver insulin *in vivo* showing exceptional performance [21,22]. Although the drug loading was easily customizable by the manufacturer through the inkjet printing technique employed, the real-time, in-situ control of the administration was still not possible.

To circumvent this pitfall, the use of a sophisticated Microelectromechanical System (MEMS) is proposed. MEMS have emerged as a valuable tool to achieve controlled and accurate brain, ocular, gastrointestinal and transdermal drug delivery [23]. Extensive work has been done on wearable insulin pumps, nonetheless these

devices must be worn constantly, and commercial insulin pumps are often avoided by diabetics due to aesthetic and practical reasons [24]. Moreover, MEMS have been integrated in close-loop systems where a sensor monitors the levels of a specific physiological signal and triggers the release of the respective therapeutic agent [25]. Although such systems are intelligent and do not require the patient to proactively manage the treatment, they must be worn or implanted. Also, they are targeted to a specific application and restricted to respond to the physiological stimulus for which they have been designed, and thus not suitable for universal drug delivery. Therefore, this work proposes an adaptable, non-wearable, stimulus-independent MEMS for administration of a variety of drug-containing solutions.

In this article we present for the first time a universal transdermal drug delivery system that combines two cutting-edge technologies, 3D printing of MNs and MEMS to create a 3DMNMEMs device. The device, consisting of a hollow MN patch integrated with a MEMS, permits the direct control of the drug administration by the user, hence enabling the personalization of treatment. Moreover, this transdermal MN-mediated approach renders the system minimally invasive and thus highly patient-compliant. The suitability of 3D printing as a fast, scalable and cost-effective technique to manufacture hollow MNs with sufficient strength for skin insertion, is demonstrated. The device was developed following a series of staggered, modular steps, starting from design, 3D printing and mechanical testing, to the usage of sophisticated optical imaging techniques to visualize the efficiency of the system in real time. Additionally, the novel 3DMNMEMS was evaluated in terms of customised drug delivery in vitro, administering a model hydrophilic molecule in different dosages. The development of the system was completed by demonstrating the efficiency of the device to administer insulin both in vitro and in vivo.

2. MATERIALS AND METHODS

2.1 Materials

The material used was a biocompatible Class I photopolymer consisting of methacrylic oligomers and phosphine oxides as photoinitiators branded as Formlabs Dental SG (GoPrint3D, North Yorkshire, UK). The insulin (aspart) (Novorapid) was bought from Novo Nordisk (London, Crawley, UK). The sodium fluorescein was purchased from Sigma Aldrich (Gillingham, Kent, UK). Streptozotocin (≥75% α-anomer basis, ≥98%) and citric

acid were both purchased from Merck Chemical Co. (Darmstadt, Germany). All solvents were of analytical grades.

2.2 Design and Additive Manufacturing of hollow MNs

The hollow MN patches were designed using the PTC Creo Computer-Aided Design software (PTC, Boston, MA, USA). The design of the patches was carried out in two stages, the first to validate the optimum MN design and the second to create a universal patch that will allow the receipt and delivery of solution. At first, hollow MN arrays were designed attached on a thin substrate of 15x15x0.5 mm. Each MN was cone-shaped with a base diameter of 1000 μm, tip diameter of 100 μm and height of 1000 μm. The hollow cone featured a wall thickness of 100 μm and the internal bores had a diameter of 800 μm at the cone base. Two MN designs, 'Bevel' and 'Ellipsis' were developed, and their printability was tested. Each array featured 49 MNs in a 7x7 symmetrical configuration. This design was employed to validate the mechanical strength and piercing capability of the MNs. Subsequently, the design was expanded, increasing the thickness of the substrate to 1.5mm and including an internal reservoir of 500μm thickness. The reservoir connected the MN bores to a 4.30mm diameter opening at the bottom of the patch, created for the provision of fluid to the MNs. The number of the MNs was reduced to 4 in a 2x2 symmetrical configuration for animal studies. The CAD models were then inserted in the Preform software (Formlabs, MA, USA). The MN patches were manufactured using the Form2 SLA 3D printer (Formlabs, MA, USA) that features high resolution capabilities (25 and 140μm for z and x, y axes, respectively). Post-printing, the arrays were purged from any unpolymerized resin residues in isopropyl alcohol bath and were then cured for 60 min at 40 °C under UV radiation using the MeccatroniCore BB Cure Dental station (GoPrint3D, UK).

2.3 Scanning Electron Microscopy (SEM)

The MN arrays were mounted onto aluminium stubs using a double-sided carbon adhesive tape (Agar Scientific, UK). Each array was examined by SEM (Hitachi SU 8030, Japan) using a low accelerating voltage (1.0 kV). A low accelerating voltage was used to avoid electrical charges on the MNs. The images were captured digitally from a fixed working distance (11.6 mm).

2.4 Preparation of porcine skin samples

Full-thickness abdominal porcine skin was collected from a local slaughterhouse (Forge Farm Ltd., Kent, UK) and was then shaved using a razor blade. The fatty tissue below the abdominal area was removed using a scalpel. Samples of full-thickness skin tissue were sliced and used for the piercing tests. The remaining skin was pinned onto a polystyrene block and wiped with ethanol (70%). Samples of 1.0±0.1 mm thickness were extracted by applying a Dermatome (Padgett Dermatome, Integra LifeTMSciences Corporation, USA) at an angle of ±45°. The thickness of the skin was measured using a caliper and 20x20 mm tissue samples were cut using a scalpel. The skin samples were placed onto filter paper soaked in a small amount of saline phosphate buffer (pH 7.4) for 2 h. The Dermatome skin samples were employed for OCT and *in vitro* release studies.

2.5 Insertion tests into porcine skin

The ability of the 3D printed hollow MNs to effectively pierce porcine skin and determine the force needed for penetration was investigated. To achieve this, the TA.XTplus Texture Analyser (Stable Micro Systems, Surrey, UK) equipped with a 5 kg load cell was employed. The MN arrays were fixed on the moving probe of the machine using double-sided adhesive tape. Samples of full-thickness abdominal skin were placed on waxed petri dishes and were secured on the bottom fixed probe of the machine. Identical 3D printed cone shaped MNs, featuring identical shape and dimensions but designed as solid, without bores and openings, were also tested, for comparison purposes. Continuous force and displacement measurements were recorded to identify the point of needle insertion. The speed of the moving probe was 0.01mm/s and all experiments were repeated 5 times.

2.6 Axial force mechanical testing

To evaluate the fracture strength of the MNs, fracture tests were conducted employing a Tinius Olsen H25KS mechanical testing machine, equipped with a 25kN load cell. The MNs were mounted on the moving probe of the machine using double-sided tape and were compressed against a flat steel plate until fracture. Moreover, identical 3D printed solid cone shaped MNs were tested, for comparison purposes. Continuous force and displacement measurements were recorded and the speed of the moving probe was 1mm/s Each experiment was repeated 5 times.

2.7 Microelectromechanical System (MEMS)

For this study, a customised diaphragmatic microdosing pump was employed (Bürkert Fluid Control Systems, Ingelfingen, Germany). The system requires connection to an electric source of 24 V that can either be supplied through a standard power source and transformer or batteries for portability. The MEMS was designed to pump single strokes of defined volume of a few microliters while allowing the tailoring of stroke frequency, mode of flow and final amount supplied. The stroke volume accuracy supplied by the MEMS was determined using a simple method. Single strokes of a solution of known concentration of sodium fluorescein salt were pumped into volumetric flasks and then diluted with deionised water. The solutions were then analyzed via UV/Vis spectrophotometry to quantify the experimental concentrations, which were then used to calculate the experimental single-stroke output. The results were compared to the expected (theoretical) concentrations based on the 5 µL value given by the manufacturer. The experiment was performed in triplicate.

2.8 X-ray Micro Computer Tomography

X-ray Micro Computer Tomography (µCT) scans were performed on the 3D printed hollow MN patch. The equipment employed was a Bruker Skyscan 1172, with an SHT 11 Megapixel camera and a Hamamatsu 80 kV (100 µA) source. The samples were mounted vertically on a portion of dental wax and positioned 259.4mm from the source. No filter was applied to the X-Ray source and a voltage of 80 kV was applied for an exposure time of 1050 ms. The images generated were 2664×4000 pixels with a resolution of 6.75 µm per pixel. The images were collected, and a volumetric reconstruction of the sample generated by Bruker's CTvol software. The threshold for this attenuation signal was set manually to eliminate speckle around the sample, and then further cleaned with a thresholding mask using Bruker's CTAn software.

2.9 Optical Coherence Tomography

The Optical Coherence Tomography (OCT) system used in this study employs a swept-source operating at a central wavelength of 1050 nm with a tuning range of roughly 100 nm, and has been described elsewhere [26]. The axial/lateral resolutions of this system during imaging were roughly 10 µm and 15 µm, respectively, with a lateral field of view of 25 × 25 mm^2. OCT data was processed using the Complex Master/Slave (CMS) method

[27]. which allowed for direct visualisation of the structures being imaged. The 3DMNMEMS device was manually compressed against a sample of full-thickness porcine skin so that the MNs were inserted into the tissue. A solution of powdered milk in water was pumped and a series of consecutive scans in equal time intervals were recorded.

2.10 In vitro release studies through porcine skin

The ability of the 3DMNMEMS device to disrupt the skin barrier and deliver molecules *in vitro* was assessed using Franz diffusion cells (PermeGear, Inc., PA, USA). Dermatomed porcine skin with a thickness of 1.0±0.1mm was employed. The skin samples were mounted on the donor compartments of a Franz diffusion cell array. The temperature of the Franz cells was maintained at 37 °C using an automated water bath (Thermo Fisher Scientific, Newington, USA). The MN patch, fitted on the MEMS, was pressed to the skin to ensure insertion. Thereafter, the MEMS was set to administer a solution of sodium fluorescein salt in deionised water (2mg/mL). Three different pumping regimes were implemented, consisting of 1, 2 and 4 serial single-stroke cycles, resulting in three different dosages: 5μL, 10 μL and 20 μL, respectively. For the samples receiving 2 and 4 strokes, fixed time intervals of 2 s were maintained between each individual stroke. Sample fractions (6–6.5 mL/h) were collected every 10 minutes using an auto-sampler (FC 204 fraction collector, Gilson, USA) attached to the Franz diffusion cells system. The experiment was repeated administering 10 μL (2 strokes) of insulin (100 IU/mL) as a bolus dose in porcine skin, and its permeation was studied for 1 hour. Statistical analysis for the drug release was performed with a Mann-Whitney nonparametric test and t-test analysis for the *in vitro* studies (InStat, GraphPad Software Inc., San Diego, CA, USA), where samples were considered as statistically significant at $p < 0.05$.

2.11 UV/Vis Spectrophotometry

The absorption spectra generated by the fluorescein sodium solutions were obtained employing 10mm path length cuvettes in a Perkin Elmer Lambda 365 at a nominal resolution of 1nm. The spectra were recorded at room temperature (20^{o}C), using deionised water as reference. The spectra were employed to quantify the concentration of the dilute.

2.12 High-performance liquid chromatography (HPLC)

The amount of insulin collected from the receptor fluid of the Franz cells was determined by HPLC (Agilent Technologies, 1200 series, Cheshire, UK) equipped with a Phenomenex Jupiter 5u c18 300 Å, LC Column (250×4.60 mm, particle size 5 µm, Macclesfield, UK). The mobile phase consisted of water with 0.1% Trifluoroacetic Acid (TFA) and acetonitrile with 0.1% TFA (66:34 v/v), with a 1 mL ml^{-1} inflow rate. The column was equilibrated at 35 °C, the injection volume was 20 µL and the eluent was analysed with a UV detector at 214 nm. The results were integrated using Chemstation® software and the samples were analysed in triplicates.

2.13 In vivo clinical studies

The effectiveness of the 3DMNMEMS device to administer insulin *in vivo* was tested on Swiss albino female mice. Before the start of the study, all animals, weighing 12 ± 10 g, were given free access to solid bottom cages with controlled diet for 3 days. To create a diabetic animal model, diabetes was chemically induced by a single subcutaneous injection of streptozotocin (50 mg/kg) in citric acid buffer (pH 4.5), in the flank. The induction of diabetes was confirmed by measuring the fasting blood glucose at scheduled times using a one-touch glucometer (ACCU-CheckVR Active, Roche, Germany), with mice that presented blood glucose higher than 300 mg/dl to be rendered diabetic. 24 h before experimentation, the diabetic animals were anesthetized and shaved on the area of 3DMNMEMS device application, using an electric razor (Panasonic, USA). Finally, the animals where fasted for 12 h, receiving only water and libitum.

On the day of experimentation, the animals were divided in 3 groups (n=6 each):

1. Untreated (negative control), received no treatment

2. SC (positive control), received 0.5 IU/animal via subcutaneous injection

3. 3DMNMEMS, received 0.5 IU/animal via the 3DMNMEMS

The animals treated with the 3DMNMEMS device were held gently while the MN array was applied on the shaved dorsal area using manual finger pressure to reassure insertion. The MEMS, connected to batteries for ease

of handling, was then fitted to the patch. The aforementioned amount of fast-acting insulin was supplied, in the form of a bolus dose, to imitate the typical subcutaneous injection treatment regime and allow the comparison thereof. After administration, the system was removed immediately. For all animal groups, blood samples from the jugular vein were collected at 0, 1, 2, 3, 4, 5 and 6 h after the insulin administration and the blood glucose values were extracted, using the glucometer. Plasma insulin concentrations were measured employing an insulin-EIA Test kit (Arbor Assays, MI, USA).

All animal experiments throughout this study were approved by the Research Ethics Committee (reference number 0003/17, Department of Pharmacy, Southern University Bangladesh) and conducted according to the Southern University Bangladesh policy for the protection of Vertebrate Animals used for Experimental and Other Scientific Purposes, with implementation of the 3Rs principle (replacement, reduction, refinement).

3. RESULTS AND DISCUSSION

3.1 3D printing of MNs

In this study, laser SLA, a photopolymerization-based technology, was employed to manufacture hollow MN patches. The desktop SLA printer featured a laser which selectively polymerizes fine “roads” (rasters) of material in a layer-by-layer fashion, on the basis of a virtual CAD model. The CAD model was inserted into a slicing software, sliced into parallel, adjacent layers and then translated into a g-code, which contained all the information necessary for the printing process. Based on the g-code, the printer used a galvano-mirror to navigate the laser in the resin vat and locally activate the photopolymerization process.

In general, 3D printing allows the fabrication of complex structures that are often unattainable through other techniques. For transdermal systems, it has the potential to replace typical manufacturing methods that are often laborious, time-consuming and difficult to customize (e.g. micromoulding). However, MNs pose an inherent challenge, due the high resolution required to accurately 3D print fine details in the microscale. Resolution in SLA printing is dependent on a number of parameters, such as the diameter of the laser beam point and the material properties. Moreover, the accuracy on the z axis is determined by the smallest step of the moving platform, while on the x and y axes, resolution is affected by the galvano-mirror movement [20]. To the authors’

knowledge, there is no scientifically sound method to predict the actual outcome of the printing process in terms of detail accuracy and dimensional fidelity to design. Improvement is mostly obtained by trial-and-error; however, the simple, user-friendly and fast nature of this technology simplifies and accelerates the prototype development.

The catalytic effect that printing resolution can have on hollow MN design and final structure was highlighted in a recent attempt to 3D print a hollow MN and microfluidic system, potentially suitable for integration in biomedical devices [28]. Albeit achieving sharp MN tips, the openings generated by the reported printing strategy were quite sizeable, possibly leading to drug losses upon application, in cases of partial skin insertion. Hence, in this work we aimed at achieving accurate printing of MNs with smaller openings, which would also be beneficial in terms of mechanical performance.

We examined the printability of two MN designs with varying placement of the bore opening, on the top ('Bevel') and side ('Ellipsis') respectively (Figure 1a, c). After printing, images acquired via SEM revealed that the formation of the top bore opening was unsuccessful, demonstrating that the model dimensions obviously exceeded the detail size that can be realized with this technology (Figure 1b). To achieve the formation of the opening, its diameter should be increased, resulting by default to decreased sharpness and thus inferior piercing capabilities [15]. On the other hand, the design featuring the side, elliptical opening generated uniform, reproducible and dimensionally faithful MNs (Figure 1d). The side bore opening was successfully printed because its position permitted the design of a larger opening within the printer resolution, without impacting the sharpness (Figure 1e).

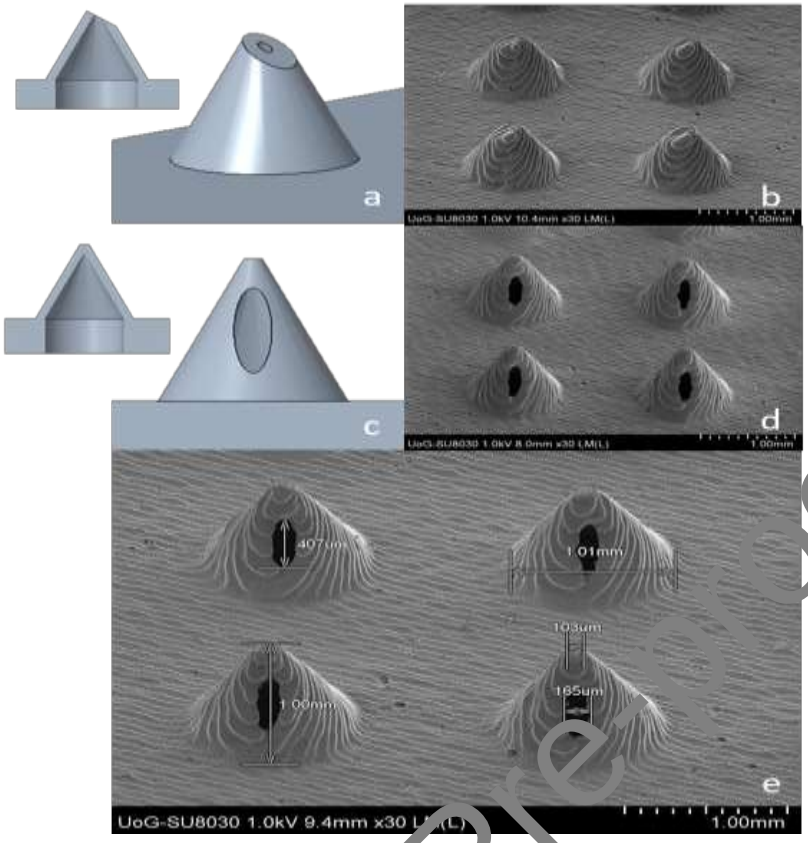

Figure 1 a,c) CAD images of the 'Bevel' and 'Ellipsis' MN designs and respective cross-sections, b,d) SEM images of the 3D printed 'Bevel' and 'Ellipsis' MNs, e) SEM image of 4 MNs of the 'Ellipsis' design featuring dimensions.

It is noteworthy that SLA MNs required no post-printing etching to sharpen the tips in contradiction to respective work using Fused Deposition Modeling (FDM), that typically features inferior resolution capabilities [29]. Thus, the production becomes faster, cheaper and easier to scale-up, while ensuring no variations on the end-product quality. Another advantage of SLA over FDM pertains on the mechanical behavior of the printed structures. On the one hand, FDM parts exhibit anisotropic and laminate-like behavior, depending on the raster (printing "road") orientation [30]. These traits add complexity to the mechanical analysis by introducing variations of the mechanical properties dependent on direction, thus complicating the design stage. Moreover, the FDM technology has been associated with poor adhesion between adjacent layers, which can lead to failure due to delamination [31]. However, it has been documented that SLA printed parts are considered isotropic [32] and delamination is not a risk associated with the SLA technology.

The superiority of this printing technology for MN manufacturing is further supported by the surface quality of the printed parts. While the characteristic layer by layer morphology, which is innate to all 3D printed structures, is visible, the MN surfaces are generally smooth. The "stair stepping" effect that has been reported elsewhere [33] is not manifested. This effect is not only visually unappealing but can also affect the mechanical performance of the MNs.

A known issue affecting the widespread adoption of 3D printing for biomedical devices is the limited selection of biocompatible, non-cytotoxic materials that are compatible with a specific printing technique. In this work, we employed a commercial Class I biocompatible resin for the printed MNs. The biocompatibility of the polymer, having been printed on a Formlabs and post-cured, has been found to conform with multiple ISO biocompatibility standards and is certified as USP IV [34], which reassures that no toxic effects were observed in acute systemic toxicity and intracutaneous testing. The claim was further supported by additional, respective studies [35,36]. The printed polymer is also autoclavable, meaning that the MNs can be sterilised.

3.2 Insertion tests into porcine skin

A critical parameter of the MN efficiency is the size of the tip since it affects the force required to penetrate the skin, which successively influences the pain induced during application [37]. It is therefore pertinent to ensure that the MNs are sharp enough to require minimal loads for penetration in order to guarantee painless application. SEM images reveal uniform tips of approximately 100 microns in diameter (Figure 1e). The specific size of tip achieved here has been investigated previously on solid MNs [21,22], showing effective piercing capabilities under minimal external loads (<5N). However, a common drawback associated with hollow MNs is their reduced strength compared to solid MNs that can hamper their performance [38]. To elucidate this, piercing tests in porcine skin were performed, recording the forces developed during piercing. As a frame of reference, identical solid microneedles were also tested. The experimental data depicted in Figure 2a are consistent with the respective literature findings [21,22]; the force-displacement curves for both solid and hollow microneedles present a constant slope at the beginning of the experiment which is associated with the elastic deformation of the skin prior to any tearing. With the increase of the applied force the slope changes although the loading remains below the threshold of 20 N, under which the skin tissue is considered purely elastic [39]. This finding is

attributed to the gradual tearing of the skin until a threshold force is reached, an event represented by a discontinuity of the curve and a drop of the force. The load increased with a steep slope after the insertion, due to the compression of the skin-MN system against the testing probe and supporting plate, in accordance with respective literature [38]. Both solid and hollow MNs exhibited a similar piercing behavior, requiring insertion forces of 1.67±0.31 N and 1.62±0.23 N, respectively. The MNs were visually inspected post-testing and no failure was reported. The skin sample was visually examined, and fine pores were observed on the piercing area (Figure 2b).

The advantage emanating from the findings of the insertion testing is twofold. The MN insertion force has been found to be directly related to the pain experienced by the patient upon application [37], hence low insertion forces is a promising indicator that the proposed hollow MN patch will cause minimal or no pain. On the other hand, minimal insertion loads facilitate self-application without the need of an applicator or the intervention of a healthcare professional. This is particularly beneficial because it increases patience-compliance and reduces treatment costs.

3.3 Axial force mechanical testing

MN damage during application is a highly undesirable event, likely to cause complications to patient health. Although there was no MN failure or damage reported during the piercing tests, to further evaluate the safety of the patches, the mechanical performance of the MNs was assessed. Axial force compressive testing was carried out on both hollow and solid MN designs against a flat metal plate and force-displacement curves were recorded.

It is noteworthy that the two designs exhibited different modes of failure; the solid fractured gradually in the direction parallel to the loading axis, while the hollow failed at the base of the cone in the direction perpendicular to the loading axis. These visual observations are also consistent with the different trends of the two curves as illustrated in Figure 2c. However, both curves showed an initial linear trend that corresponds to the loads that the MNs withstood without plastic deformations. This linearity designates a load range within which the MNs maintain their structural integrity, with thresholds of 98.2±4.6 N and 366.3±4.4 N, for the hollow and solid MNs, respectively. As expected, the solid MNs were able to withstand higher loads before yield compared to the

hollow ones; however, both yield points corresponded to forces that are well above the respective loads required for insertion to skin.

Combining both data sets, the margin of safety of the MNs, which is defined as the ratio of the fracture force to the insertion force [40], is calculated as 220 for the solid and 60 for the hollow MNs. Given that both numbers are significantly higher than 1, the safety of the MNs is reassured. Furthermore, the aforementioned values are significantly higher compared to respective findings in literature. Forvi et al. reported margins of safety ranging between 6 and 9 for solid silicon MNs [41], while Davis et al. calculated values between 5 and 20 for polymeric hollow MNs [38]. The comparatively increased margins of safety generated by the MNs proposed in this study are attributed to the high strength of the polymer [42] combined to the increased sharpness of the tips.

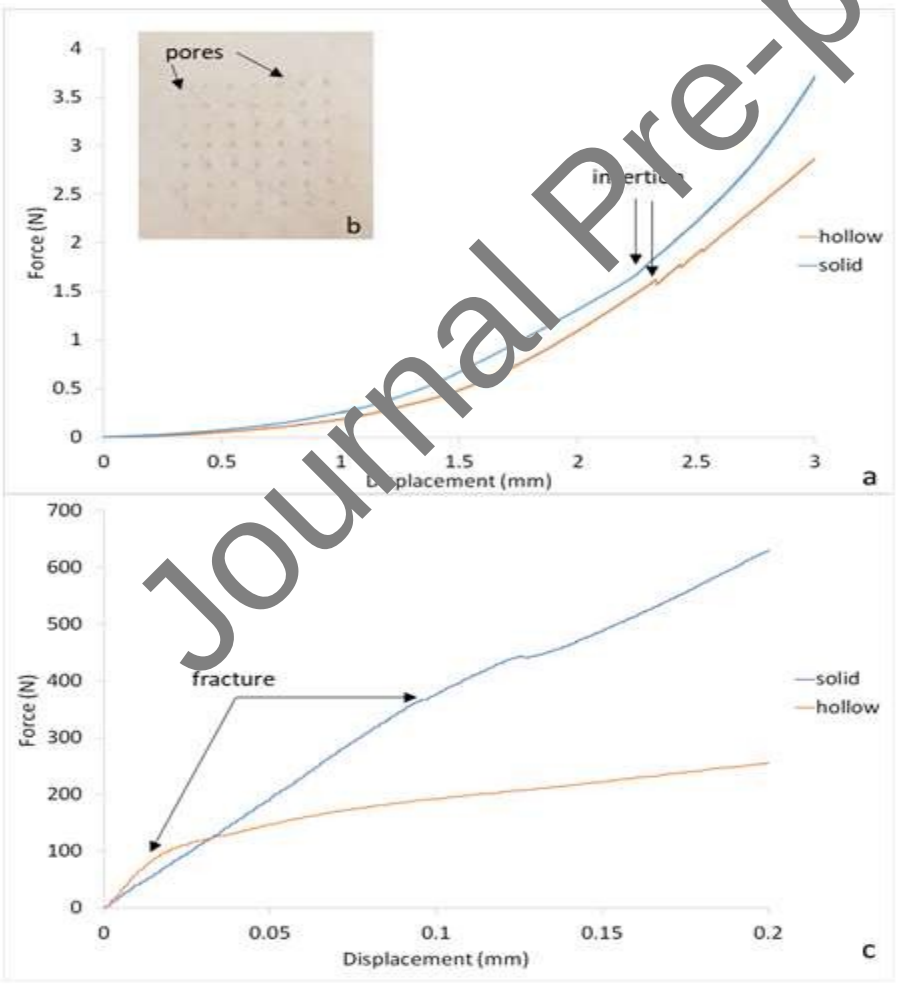

Figure 2 a) Force vs displacement curve obtained from MN piercing tests in porcine skin for hollow and identical solid MNs using a Texture Analyzer, b) pores in porcine skin after piercing test, c) Force vs displacement curve obtained from MN fracture testing against a flat metal plate

3.4 Development of the 3DMNMEMS and accuracy evaluation

In this study, we coupled the 3D printed MNs with a diaphragmatic micropump as a MEMS, to create a 3D printed MN-mediated drug delivery system. The rationale behind selecting a MEMS over other strategies to stimulate flow through hollow MNs, such as coupling with typical syringes [43,44], was to accomplish high dose accuracy and reproducibility. Furthermore, the MEMS enables the tailoring of the delivery process by the user through simple settings, while its handling is effortless and user-friendly.

The MEMS was designed to pump very small volumes of fluid, down to a few microliters, with a defined volume per stroke, allowing the tailoring of frequency (from 5 up to 40 Hz) and mode of dosing (continuous, single stroke etc.). The micropump features three valves operating as the inlet, outlet and pumping diaphragm valves and is designed to pump strokes of 5 μL in volume.

Inaccuracies of typical drug delivery methods such as syringes or pen-injectors, especially for small dosages, have been well-documented [45]. To verify the accuracy of the MEMS in regard to the volume of a single stroke, a simple method was developed using a fluorescein salt solution of known concentration. Single strokes of the solution were pumped into volumetric flasks and then diluted with deionized water. UV/Vis spectrophotometry measurements generated the respective experimental concentration, which was used to calculate the single stroke volume that was initially pumped into the solution (v_{exp}). The experimental volume was compared to the theoretical volume, v_{theor}, of 5 μL according to the manufacturer. The single stroke volume % error was calculated by Equation (1):

Where v_{theor} and v_{exp} the theoretical and experimental volumes of a single stroke. The error was calculated as 7.9±0.82% and the value was used to correct the calculations throughout this study, so they correspond to the real volumes supplied by the MEMS. The error value is acceptably low, particularly when compared with syringes, that have been found to overdose with an error of up to 23% for small dosages [45]. The low standard deviation of the average highlights the accuracy of the MEMS in terms of the volume supplied, which is of paramount importance for applications wherein high precision is aimed at.

In order to combine the MN arrays with the MEMS, a patch featuring a tubular opening at its base and an internal reservoir to connect it to the MN bores, was designed and 3D printed (Figure 3a). The design allows fluid to enter through the opening to the internal reservoir and from there to be dispersed to the MN bores. The final patch has been designed to secure a tight fit between the MN patch and the micropump, in order to prohibit liquid losses at the point of connection, while allowing the easy attachment and changing of the MN patches between uses (Figure 3e).

3.5 X-ray Micro Computer Tomography (μCT)

An innate drawback of SLA printing of structures that feature internal cavities is associated with imperfect cleaning of unpolymerized resin residues. In this event, the residues solidify during post-printing curing and can partially or fully block the internal channels and reservoir and thus hamper the fluid delivery. To investigate the quality of the internal cavities and reassure uniform dispersion of the solution supplied by the MEMS, μCT was employed as a sophisticated, non-destructive technique to image the internal geometry. Figure 3c illustrates a perpendicular cross-section of the patch along the central axis of two MNs; it is evident that the internal surface appears smooth with no polymerized residues and blockages in MN bores, internal tank and tubular opening. This is further verified by the scan of the horizontal cross-section at the base of the MNs, where the bores are shown circular without significant alterations to their geometry caused by solidified residues (Figure 3d). These findings suggest that there are no imperfections to the patch introduced by the printing technology that can affect its performance as a drug delivery system.

3.6 Optical Coherence Tomography

A well-documented issue associated with hollow MNs, stems from the dense nature of the skin tissue which, being compressed during piercing, may hinder the infusion and dispersion of liquid formulation [46]. To investigate the performance of the 3DMNMEMS device on this area, Optical Coherence Tomography (OCT) was employed in an attempt to visualize the liquid transfer from the MNs to the skin tissue. OCT is a valuable non-destructive, non-invasive technique that captures images from within a sample, based on the capturing of low-coherence light variations reflected. It has been used extensively for biomedical imaging [47,48] and imaging of MN piercing behavior into skin [49,50]. However, to the authors' knowledge, real-time capturing of

liquid infusion from hollow MNs inserted into biological skin tissue has not been previously reported. Here, we present for the first time, an in situ, real-time visualization of liquid being administered by our 3DMNMEMS device within the porcine skin.

The MN component of the device was inserted into a sample of porcine skin. Figure 3f shows a pre-pumping image of a lateral cross-section that depicts the insertion of approximately 70% of the total MN length (700 μm). These measurements are in agreement with respective ones derived via μCT when solid MNs of similar geometry were inserted into 5 plies of parafilm [22]. The insertion depth reported here along with the design of the MN that places the lowest point of the elliptical opening at 300 μm away from the base, suggest that upon application the MN opening will be entirely within the skin tissue. This minimizes the possibility of fluid escaping and remaining on the skin surface.

Thereafter, consecutive images of a horizontal cross-section of the skin during liquid pumping were captured, at the depth of the MN side opening. The images were captured perpendicular to the needle in order to allow the imaging of the fluid diffusing from the side opening of the hollow MNs. Figure 3g-j illustrates the real-time progressive infusion of the liquid and its propagation within the tissue (video is available as Supplementary Material). Evidently, the solution is distributed in an advancingly broader angle which suggests better liquid diffusion. This visual evidence suggests that there is no creation of fluid depots within the skin that typically slow down drug absorption and thus strengthen the hypothesis that the 3DMNMEMS device is a promising system for efficacious transdermal drug delivery.

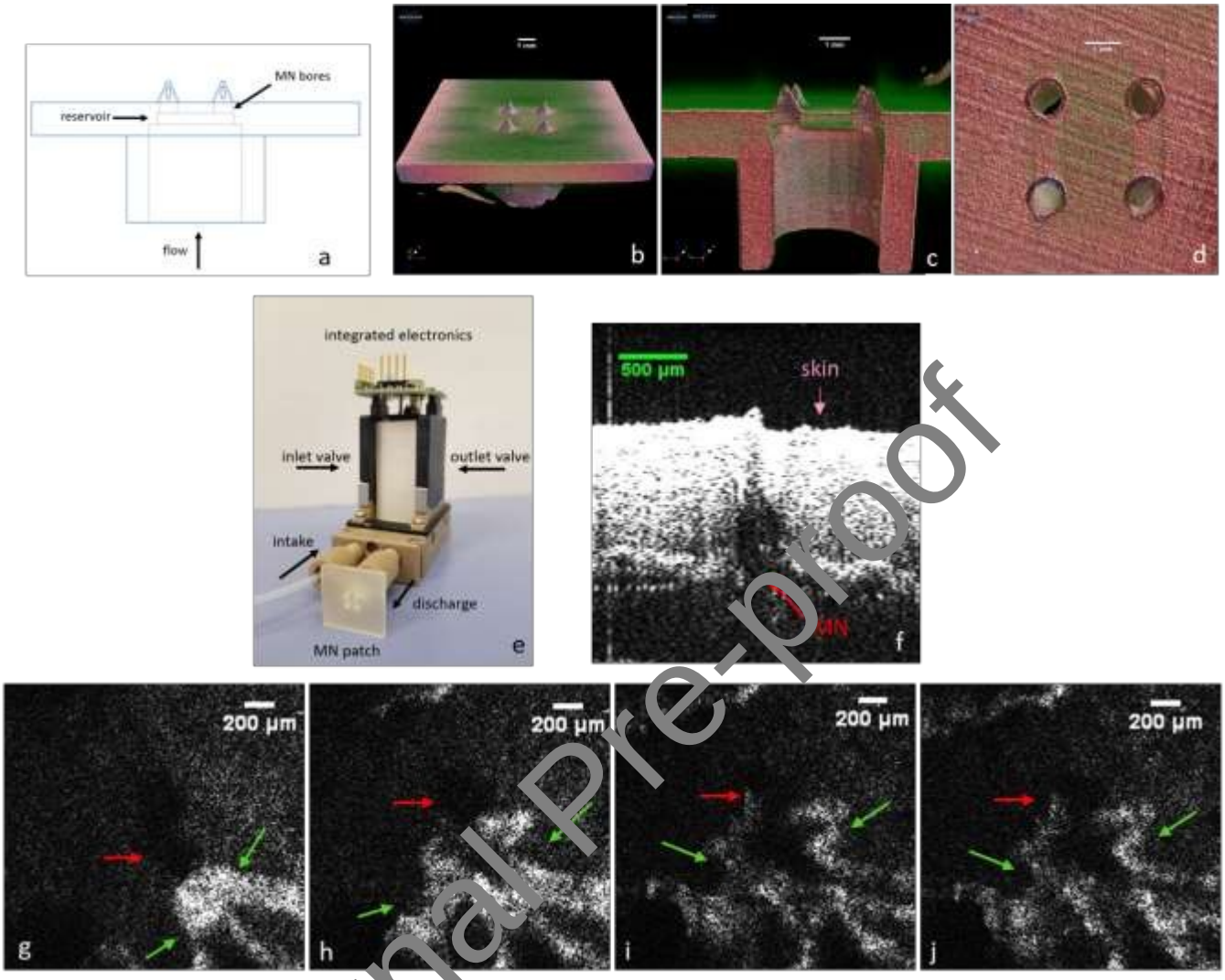

Figure 3 a) Scheme of the hollow MN patch featuring an internal reservoir for liquid delivery, b-d) µCT images of the hollow MN patch that reveal that internal structures have been printed accurately and no internal blockages will obstruct fluid circulation, e) 3DMNMEMS configuration, f) OCT image of a MN inserted in a sample of full thickness porcine skin, g-j) OCT captions of the progressive distribution of liquid solution (marked with green arrows) delivered from a single MN (red arrows indicate the MN tip) within porcine skin tissue (video available in Supplementary material).

3.7 In vitro release through porcine skin

Prior to animal testing, we proceeded to test the performance of the device to disrupt the skin barrier and deliver drugs *in vitro*, using Franz diffusion cells. Initially, we studied the release of different dosages of sodium fluorescein salt in porcine skin, as a model hydrophilic molecule. The skin samples were pierced with the 3DMNMEMS and three different dosages of 5 µL, 10 µL and 20 µL were administered. After analysis and quantification via UV/Vis spectroscopy, it was found that for all dosages, 100% of the amount administered was detected in the receptor compartment in 30 minutes (Figure 4a). The release was faster as the dosage increased,

with almost 100% of the fluorescein salt detected in the receptor compartment in 20 min for dosages of 10 and 20 μL. The fluorescein was found to be released earlier as the dosage increased because with additional pumping, the solution is forced to diffuse further into the skin. As demonstrated by the findings of the OCT study, the 3DMNMEMS creates a network of microchannels in the skin, that propagates with each additional stroke. The network is more likely to spread all the way to the receptor compartment with more strokes, creating an interconnecting pathway with the MN, accelerating thus drug diffusion.

Thereafter, the release of insulin in porcine skin was also examined. As seen in Figure 4b, a single dosage of 10 μL (0.5 IU) was fully detected in the receptor compartment in 1 hour. The release of insulin is slightly slower as anticipated given the large molecular size of the insulin molecule which slows down the diffusion to the dermal microcirculation.

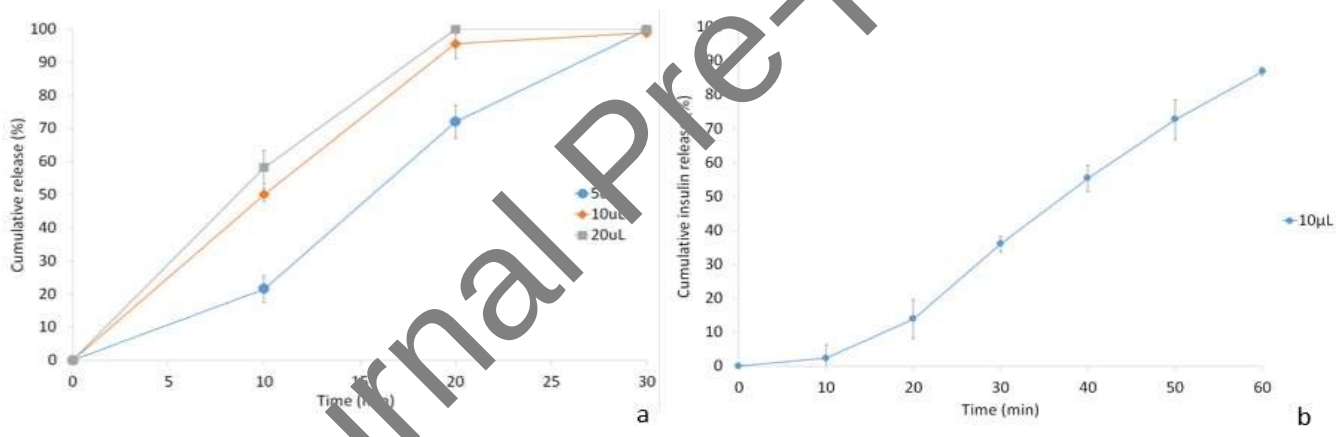

Figure 4 Cumulative *in vitro* release generated by the 3DMNMEMS of a) sodium fluorescein salt and b) insulin in porcine skin.

3.8 In vivo clinical studies

The ability of the 3DMNMEMS device to administer insulin *in vivo* was investigated using a diabetic animal model, under the protocol described in the experimental section. Diabetes was confirmed after 7 days of streptozotocin administration. The preliminary diabetes (hyperglycemia) was shown as 340 ± 10 mg/dl. The diabetic mice were divided into three groups: Untreated (negative control), subcutaneously (SC) injected (positive control) and treated with the 3DMNMEMS device (same amount as SC injection). For the latter, the system was applied on shaved dorsal skin inserting the MN patch using manual finger pressure (Figure 5b-c). The MEMS was then coupled with the MN patch and 0.5 IU were administered. Albeit the assembled device can

be readily applied on skin, conducting the application in two discreet steps enabled better control of the pressure applied on the animals. Skin pores were observed after MN removal which disappeared after 5 minutes (Figure 5e-f).

The dose of 0.5 IU was selected in order to avoid hypoglycemia in mice for 6 h. The plasma glucose levels detected at each group are shown in Figure 5g. The 3DMNMEMS device demonstrated a similar release pattern as the SC group. However, it was found that the device facilitated a rapid decrease of the blood glucose levels compared to its initial value within 1 hour whereas for the SC the respective minimum was reached in 3 hours. This is owed to the fact that the injection forms a depot within the interstitial space the content of which is slowly released due to passive diffusion. This finding further supports the OCT results that display broad liquid distribution within the skin tissue. Evidently, the device seems to enable the circumvention of a known limitation associated with the delivery of insulin via subcutaneous injection: the production of back pressure that retards drug distribution for absorption.

Along the same lines, significant improvement in terms of onset action is observed in comparison with other hollow MN systems tested for insulin delivery [15,51,52]. As shown by these studies, the effect of the insulin administered manifests gradually and the blood glucose minima are detected around 4 to 5 hours after administration. There is robust evidence that the comparative advantage of the 3DMNMEMS stems from the swift and broad liquid distribution within the skin tissue, induced by the pumping. Hence, the drug absorption does not rely on passive diffusion kinetics which play an important role in typical hollow MN-mediated drug delivery.

Figure 5h depicts the plasma insulin concentration which are in agreement with the reduction of plasma glucose. Based on the data derived from the *in vivo* studies, the minimum value of blood glucose (C_{min}) as well as the respective time point (T_{min}) were obtained from the plasma glucose vs time curve. The relative pharmacological availability (RPA) was calculated from Equation (2):

Where $AAC_{3DMNMEMS}$ and AAC_{sc} are the areas above the curve after insulin administration via the 3DMNMEMS device and subcutaneous injection respectively and $dose_{sc}$ and $dose_{3DMNMEMS}$ are the respective dosages.

Table 1 Pharmacodynamic parameters of insulin administration

	Pharmacodynamic parameters			
	C_{min} (%)	t_{min} (h)	AAC_{0-6h}	RPA (%)
Untreated	100	0	0	0
SC	29.92	3	323.75	100
3DMNMEMS	29.47	1	340.4	105.14

The plasma insulin concentration vs time curve generated the maximum insulin concentration (C_{max}) as well as the respective time point (T_{max}). Equation (3) was used to calculate the relative bioavailability (RBA):

Where $AUC_{3DMNMEMS}$ and AUC_{sc} are the areas under the curve after insulin administration via the 3DMNMEMS device and subcutaneous injection respectively and $dose_{sc}$ and $dose_{3DMNMEMS}$ are the respective dosages.

Table 2 Pharmacokinetic parameters of insulin administration

	Pharmacokinetic parameters			
	C_{max} (μIU/mL)	t_{min} (h)	AUC_{0-6h}	RBA (%)
Untreated	0	0	0	0
SC	73.24	3	284.3	100
3DMNMEMS	71.6	1	274.95	96.71

The RPA values calculated in this study (Table 1), reveal that insulin administered by the 3DMNMEMS device has an enhanced pharmacological effect reducing blood glucose compared to the injection-administered one. On the other hand, the RBA of 96.71% (Table 2) suggests that there is a slightly smaller insulin absorption in the 3DMNMEMS-treated group in the duration of the study. This is further supported by the trend of the plasma insulin concentration curve (Figure 5h). While the respective data from the SC group show that the insulin concentration presents a steep decrease towards the end of the study (9 μIU/mL at 6 hours after treatment), the plasma insulin concentration of the 3DMNMEMS group shows a more moderate decrease (16.1 μIU/mL at 6 hours after treatment). This finding suggests that the insulin absorption in the 3DMNMEMS-treated group continued beyond the 6-hour duration of the experiment, evincing a more sustained insulin action.

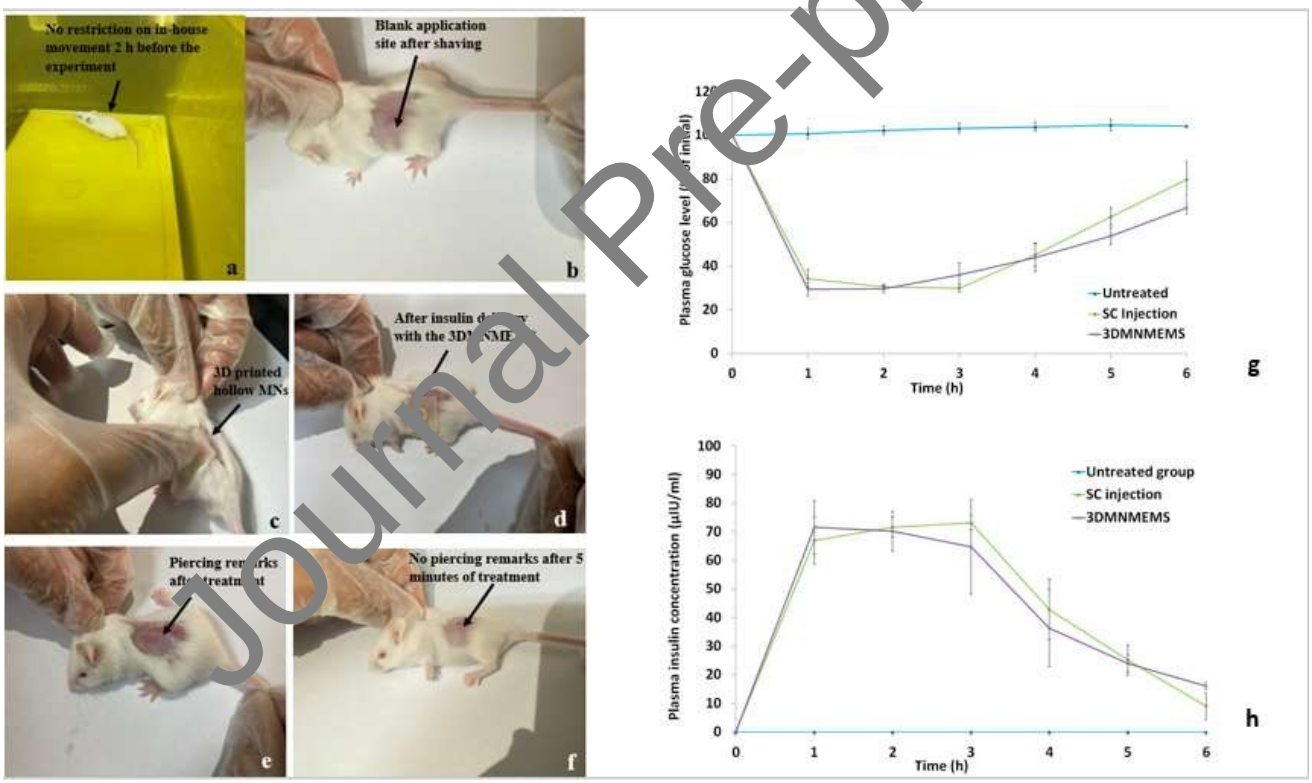

Figure 5 *In vivo* animal studies using a diabetic mice model for the treatment of diabetes using the 3DMNMEMS. a) No restriction of in-house movement 2 hours prior to the experiment, b) blank application site after shaving, c) application of the 3D printed hollow MN patch, d) after insulin delivery using the 3DMNMEMS, e) after-piercing pores after treatment, f) No pores 5 minutes after treatment, g) plasma glucose levels after insulin administration, h) plasma insulin concentation after insulin administration.

4. CONCLUSIONS

In this paper, 3D printed MNs and MEMS were combined to develop a novel system for universal transdermal drug delivery. The system allows the in-situ control of drug administration by the user, rendering the system a valuable tool for personalization of treatment. We demonstrated that SLA, a cost-effective 3D printing technology generates uniform, reproducible and sharp hollow MNs. The MNs were found to effectively pierce the skin requiring minimal loads which associates with minimal pain and easy self-application. The high fracture strength of the MNs reassured that they are safe during application. Employing advanced optical imaging techniques, we were able to monitor liquid being diffused from the 3DMNMEMS in real time within skin tissue. It was shown that the system facilitated broad distribution of the liquid without the creation of depots, thus accelerating drug absorption. *In vivo* clinical trials of insulin administration to diabetic animals illustrated that the 3DMNMEMS achieved slightly faster insulin onset action and prolonged duration of glycemic control compared to subcutaneous injection, but in a painless manner.

The platform device presented in this work was not designed to respond to a specific stimulus, e.g. glucose level, but leaves the full control of the administration process to the user. This practically entails that a range of drugs, suitable for transdermal delivery, can be delivered through this approach. Along the same lines, the device can be potentially utilised for the delivery of vaccines, to harvest the well-documented advantages of hollow MN-mediated vaccine delivery. Hence, new pathways are opened and limitations of MN based systems, e.g. fixed cargo amount for dissolvable and coated MNs, are circumvented, maintaining the benefits of MN-mediated delivery. Overall, this work demonstrates that the integration of MEMS with 3D printing can be a key to the evolution of medical devices for personalized treatment.

REFERENCES

[1] D.J.A. Crommelin, G. Storm, P. Luijten, "Personalised medicine" through "personalised medicines": Time to integrate advanced, non-invasive imaging approaches and smart drug delivery systems, Int. J. Pharm. 415 (2011) 5–8. https://doi.org/10.1016/j.ijpharm.2011.02.010.

[2] G. Chen, Y. Xu, P. Kwok, L. Kang, Pharmaceutical Applications of 3D Printing, Addit. Manuf. (2020). https://doi.org/https://doi.org/10.1016/j.addma.2020.101209.

[3] S.J. Trenfield, A. Awad, C.M. Madla, G.B. Hatton, J. Firth, A. Goyanes, S. Gaisford, A.W. Basit, Shaping the future: recent advances of 3D printing in drug delivery and healthcare, Expert Opin. Drug Deliv. (2019). https://doi.org/10.1080/17425247.2019.1660318.

[4] J.A. Weisman, D.H. Ballard, U. Jammalamadaka, K. Tappa, J. Sumerel, D.K. Mills, P.K. Woodard, F. Park, 3D printed antibiotic and chemotherapeutic eluting catheters for potential use in interventional radiology: in vitro proof of concept study, Acad Radiol. 26 (2019) 270–274. https://doi.org/10.1016/j.acra.2018.03.022.

[5] S.A. Stewart, J. Domínguez-Robles, V.L. McIlorum, E. Mancuso, D.A. Lamprou, R.F. Donnelly, E. Larrañeta, Development of a biodegradable subcutaneous implant for prolonged drug delivery using 3D printing, Pharmaceutics. 12 (2020). https://doi.org/10.3390/pharmaceutics12020105.

[6] J. Domínguez-Robles, C. Mancinelli, E. Mancuso, I. García-Romero, B.F. Gilmore, L. Casettari, E. Larrañeta, D.A. Lamprou, 3D printing of drug-loaded thermoplastic polyurethane meshes: A potential material for soft tissue reinforcement in vaginal surgery, Pharmaceutics. 12 (2020). https://doi.org/10.3390/pharmaceutics12010063.

[7] N. Noor, A. Shapira, R. Edri, I. Gal, L. Wertheim, T. Dvir, 3D Printing of Personalized Thick and Perfusable Cardiac Patches and Hearts, Adv. Sci. 6 (2019). https://doi.org/10.1002/advs.201900344.

[8] S. Kotta, A. Nair, N. Alsabeelah, 3D Printing Technology in Drug Delivery: Recent Progress and Application, Curr. Pharm. Des. (2018). https://doi.org/10.2174/1381612825666181206123828.

[9] M. Di Prima, J. Coburn, D. Hwang, J. Kelly, A. Khairuzzaman, L. Ricles, Additively manufactured medical products – the FDA perspective, 3D Print. Med. 2 (2015) 1. https://doi.org/10.1186/s41205-016-0005-9.

[10] M.R. Prausnitz, R. Langer, Transdermal drug delivery, Nat. Biotechnol. 26 (2009) 1261–1268. https://doi.org/10.1038/nbt.1504.Transdermal.

[11] H. Lee, C. Song, S. Baik, D. Kim, T. Hyeon, D.H. Kim, Device-assisted transdermal drug delivery, Adv. Drug Deliv. Rev. 127 (2018) 35–45. https://doi.org/10.1016/j.addr.2017.08.009.

[12] A.Z. Alkilani, M.T.C. McCrudden, R.F. Donnelly, Transdermal drug delivery: Innovative pharmaceutical developments based on disruption of the barrier properties of the stratum corneum, Pharmaceutics. 7 (2015) 438–470. https://doi.org/10.3390/pharmaceutics7040438.

[13] T. Waghule, G. Singhvi, S.K. Dubey, M.M. Pandey, G. Gupta, M. Singh, K. Dua, Microneedles: A smart approach and increasing potential for transdermal drug delivery system, Biomed. Pharmacother. 109 (2019) 1249–1258. https://doi.org/10.1016/j.biopha.2018.10.078.

[14] A. McConville, C. Hegarty, J. Davis, Mini-Review: Assessing the Potential Impact of Microneedle Technologies on Home Healthcare Applications, Medicines. 5 (2018) 50. https://doi.org/10.3390/medicines5020050.

[15] P.M. Wang, M. Cornwell, J. Hill, M.R. Prausnitz, Precise microinjection into skin using hollow microneedles, J. Invest. Dermatol. 126 (2006) 1080–1087. https://doi.org/10.1038/sj.jid.5700150.

[16] S.N. Economidou, D.A. Lamprou, D. Douroumis, 3D printing applications for transdermal drug delivery, Int. J. Pharm. 544 (2018) 415–424. https://doi.org/10.1016/j.ijpharm.2018.01.031.

[17] Z. Faraji Rad, R.E. Nordon, C.J. Anthony, L. Bilston, P.D. Prewett, J.Y. Arns, C.H. Arns, L. Zhang, G.J. Davies, High-fidelity replication of thermoplastic microneedles with open microfluidic channels, Microsystems Nanoeng. 3 (2017) 1–11. https://doi.org/10.1038/micronano.2017.34.

[18] A. Ovsianikov, B. Chichkov, P. Mente, N.A. Monteiro-Riviere, A. Doraiswamy, R.J. Narayan, Two

Photon Polymerization of Polymer Ceramic Hybrid Materials for Transdermal Drug Delivery, Int. J. Appl. Ceram. Technol. 4 (2007) 22–29. https://doi.org/10.1111/j.1744-7402.2007.02115.x.

[19] K. Moussi, A. Bukhamsin, T. Hidalgo, J. Kosel, Biocompatible 3D Printed Microneedles for Transdermal, Intradermal, and Percutaneous Applications, Adv. Eng. Mater. 22 (2020) 1–10. https://doi.org/10.1002/adem.201901358.

[20] C. Schmidleithner, D.M. Kalaskar, Stereolithography, in: IntechOpen, 2018. https://doi.org/http://dx.doi.org/10.5772/57353.

[21] C.P.P. Pere, S.N. Economidou, G. Lall, C. Ziraud, J.S. Boateng, B.D. Alexander, D.A. Lamprou, D. Douroumis, 3D printed microneedles for insulin skin delivery, Int. J. Pharm. 544 (2018) 425–432. https://doi.org/10.1016/j.ijpharm.2018.03.031.

[22] S.N. Economidou, C.P.P. Pere, A. Reid, M.J. Uddin, W.C. Windmill, D.A. Lamprou, D. Douroumis, 3D printed microneedle patches using stereolithography (SLA) for intradermal insulin delivery, Mater. Sci. Eng. C. 102 (2019) 743–755. https://doi.org/10.1016/j.msec.2019.04.063.

[23] H.J. Lee, N. Choi, E.S. Yoon, I.J. Cho, MEMS devices for drug delivery, Adv. Drug Deliv. Rev. 128 (2018) 132–147. https://doi.org/10.1016/j.addr.2017.11.003.

[24] C. Robertson, A. Lin, G. Smith, A. Yeung, P. Strauss, J. Nicholas, E. Davis, T. Jones, L. Gibson, J. Richters, M. de Bock, The Impact of Externally Worn Diabetes Technology on Sexual Behavior and Activity, Body Image, and Anxiety in Type 1 Diabetes, J. Diabetes Sci. Technol. (2019). https://doi.org/10.1177/1932296819870541.

[25] J. Yu, Y. Zhang, A.R. Kahkoska, Z. Gu, Bioresponsive transcutaneous patches, Curr. Opin. Biotechnol. 48 (2017) 28–32. https://doi.org/10.1016/j.copbio.2017.03.001.

[26] M.J. Marques, S. Rivet, A. Bradu, A. Podoleanu, Complex master-slave for long axial range swept-source optical coherence tomography, OSA Contin. 1 (2018) 1251. https://doi.org/10.1364/osac.1.001251.

[27] S. Rivet, M. Maria, A. Bradu, T. Feuchter, L. Leick, A. Podoleanu, Complex master slave interferometry,

Opt. Express. 24 (2016) 2885. https://doi.org/10.1364/oe.24.002885.

[28] C. Yeung, S. Chen, B. King, H. Lin, K. King, F. Akhtar, G. Diaz, B. Wang, J. Zhu, W. Sun, A. Khademhosseini, S. Emaminejad, A 3D-printed micro fluidic-enabled hollow microneedle architecture for transdermal drug delivery, Biomicrofluidics. 13 (2019) 064125. https://doi.org/10.1063/1.5127778.

[29] M.A. Luzuriaga, D.R. Berry, J.C. Reagan, R.A. Smaldone, J.J. Gassensmith, Biodegradable 3D printed polymer microneedles for transdermal drug delivery, Lab Chip. 18 (2018) 1223–1230. https://doi.org/10.1039/c8lc00098k.

[30] A. Dey, N. Yodo, A Systematic Survey of FDM Process Parameter Optimization and Their Influence on Part Characteristics, J. Manuf. Mater. Process. 3 (2019) 64. https://doi.org/10.3390/jmmp3030064.

[31] T.N.A.T. Rahim, A.M. Abdullah, H. Md Akil, Recent Developments in Fused Deposition Modeling-Based 3D Printing of Polymers and Their Composites, Polym. Rev. 59 (2019) 589–624. https://doi.org/10.1080/15583724.2019.1597889.

[32] J.R.C. Dizon, A.H. Espera, Q. Chen, R.C. Advincula, Mechanical characterization of 3D-printed polymers, Addit. Manuf. 20 (2018) 44–67. https://doi.org/10.1016/j.addma.2017.12.002.

[33] A.R. Johnson, A.T. Procopio, Low cost additive manufacturing of microneedle masters, 3D Print. Med. 5 (2019). https://doi.org/10.1186/s41205-019-0039-x.

[34] Vertex, Certificate of Biocompatibility, 2016. https://support.formlabs.com/s/article/Certifications-and-standards?language=en_US.

[35] C. Kurzmann, K. Janjić, H. Shokoohi-Tabrizi, M. Edelmayer, M. Pensch, A. Moritz, H. Agis, Evaluation of Resins for Stereolithographic 3D-Printed Surgical Guides: The Response of L929 Cells and Human Gingival Fibroblasts, Biomed Res. Int. 2017 (2017). https://doi.org/10.1155/2017/4057612.

[36] S. Kreß, R. Schaller-Ammann, J. Feiel, J. Priedl, C. Kasper, D. Egger, 3D printing of cell culture devices: Assessment and prevention of the cytotoxicity of photopolymers for stereolithography, Materials (Basel). 13 (2020). https://doi.org/10.3390/ma13133011.

[37] H.S. Gill, D.D. Denson, B.A. Burris, M.R. Prausnitz, Effect of microneedle design on pain in human subjects, Clin J Pain. 24 (2008) 585–594. https://doi.org/10.1097/AJP.0b013e31816778f9.Effect.

[38] S.P. Davis, B.J. Landis, Z.H. Adams, M.G. Allen, M.R. Prausnitz, Insertion of microneedles into skin: Measurement and prediction of insertion force and needle fracture force, J. Biomech. 37 (2004) 1155–1163. https://doi.org/10.1016/j.jbiomech.2003.12.010.

[39] C. Pailler-Mattei, S. Bec, H. Zahouani, In vivo measurements of the elastic mechanical properties of human skin by indentation tests, Med. Eng. Phys. 30 (2008) 599–606. https://doi.org/10.1016/j.medengphy.2007.06.011.

[40] M.R. Prausnitz, Microneedles for transdermal drug delivery, Adv. Drug Deliv. Rev. 56 (2004) 581–587. https://doi.org/10.1016/j.addr.2003.10.023.

[41] E. Forvi, M. Soncini, M. Bedoni, F. Rizzo, M. Carelli, C. O'Mahony, F. Gramatica, A method to determine the margin of safety for microneedle arrays, WCE 2010 - World Congr. Eng. 2010. 2 (2010) 1550–1554.

[42] Formlabs, Dental SG Material Properties, 2016.

[43] B. Stoeber, D. Liepmann, Arrays of hollow out-of-plane microneedles for drug delivery, J. Microelectromechanical Syst. 14 (2005) 472–479. https://doi.org/10.1109/JMEMS.2005.844843.

[44] I. Mansoor, Y. Liu, U.O. Häfeli, B. Stoeber, Arrays of hollow out-of-plane microneedles made by metal electrodeposition onto solvent cast conductive polymer structures, J. Micromechanics Microengineering. 23 (2013). https://doi.org/10.1088/0960-1317/23/8/085011.

[45] M.G. Gnanalingham, P. Newland, C.P. Smith, Accuracy and reproducibility of low dose insulin administration using pen-injectors and syringes, Arch. Dis. Child. 79 (1998) 59–62. https://doi.org/10.1136/adc.79.1.59.

[46] W. Martanto, J.S. Moore, O. Kashlan, R. Kamath, P.M. Wang, J.M. O'Neal, M.R. Prausnitz, Microinfusion using hollow microneedles, Pharm. Res. 23 (2006) 104–113.

https://doi.org/10.1007/s11095-005-8498-8.

[47] J.G. Fujimoto, C. Pitris, S.A. Boppart, M.E. Brezinski, Optical coherence tomography: An emerging technology for biomedical imaging and optical biopsy, Neoplasia. 2 (2000) 9–25. https://doi.org/10.1038/sj.neo.7900071.

[48] J. Walther, M. Gaertner, P. Cimalla, A. Burkhardt, L. Kirsten, S. Meissner, E. Koch, Optical coherence tomography in biomedical research, Anal. Bioanal. Chem. 400 (2011) 2721–2743. https://doi.org/10.1007/s00216-011-5052-x.

[49] R.F. Donnelly, M.J. Garland, D.I.J. Morrow, K. Migalska, T.R.R. Singh, R. Majithiya, A.D. Woolfson, Optical coherence tomography is a valuable tool in the study of the effects of microneedle geometry on skin penetration characteristics and in-skin dissolution, J. Control. Release. 147 (2010) 333–341. https://doi.org/10.1016/j.jconrel.2010.08.008.

[50] R.F. Donnelly, K. Mooney, M.T.C. McCrudden, E.M. Vicente-Pérez, L. Belaid, P. González-Vázquez, J.C. McElnay, A.D. Woolfson, Hydrogel-forming microneedles increase in volume during swelling in skin , but skin barrier function recovery is unaffected, J Pharm Sci. 103 (2014) 1478–1486. https://doi.org/10.1002/jps.23921. Hydrogel-forming.

[51] S.P. Davis, W. Martanto, M.G. Allen, S. Member, M.R. Prausnitz, Hollow Metal Microneedles for Insulin Delivery to Diabetic Rats, 52 (2005) 909–915.

[52] D. V Mcallister, P.M. Wang, S.P. Davis, J. Park, P.J. Canatella, M.G. Allen, M.R. Prausnitz, Microfabricated needles for transdermal delivery of macromolecules and nanoparticles : Fabrication methods and transport studies, 100 (2003) 13755–13760.

Authorship contributions:

Conceptualization: Sophia N. Economidou, Dennis Douroumis

Data curation: Sophia N. Economidou, Andrew Reid, Manuel J. Marques, Md. Jasim Uddin

Formal analysis: Sophia N. Economidou, Andrew Reid, Manuel J. Marques, Md. Jasim Uddin

Methodology: Sophia N. Economidou, Md. Jasim Uddin, Manuel J. Marques, Dennis Douroumis, Wan Ting Sow, Huaqiong Li, Andrew Reid, James F.C. Windmill, Adrian Podoleanu

Project administration: Sophia N. Economidou, Dennis Douroumis, Adrian Podoleanu

Resources: Dennis Douroumis, Md. Jasim Uddin, Adrian Podoleanu

Supervision: Dennis Douroumis, Huaqiong Li, Adrian Podoleanu

Validation: Sophia N. Economidou, Md. Jasim Uddin, Dennis Douroumis, Huaqiong Li, Adrian Podoleanu

Visualization: Sophia N. Economidou, Manuel J. Marques, Andrew Reid, James F.C. Windmill, Md. Jasim Uddin

Roles/Writing - original draft: Sophia N. Economidou

Declaration of interests

☒ The authors declare that they have no known competing financial interests or personal relationships that could have appeared to influence the work reported in this paper.

☐The authors declare the following financial interests/personal relationships which may be considered as potential competing interests: